**This is a preprint version of the conference paper published in : Proceedings of the ASME 2023 International Mechanical Engineering Congress and Exposition. Volume 12: Micro- and Nano-Systems Engineering and Packaging. New Orleans, Louisiana, USA. October 29–November 2, 2023. V012T13A023. ASME.
The final version is available via DOI: https://doi.org/10.1115/IMECE2023-111722

COMPARATIVE ELECTRODE DESIGN FOR PIEZOELECTRIC MEMS KINETIC ENERGY HARVESTER

Ranjith D. Janardhana [1] and Nathan Jackson [1,2]

[1]Department of Mechanical Engineering, University of New Mexico, Albuquerque, NM, USA
[2]Nanoscience and Microsystems Engineering, University of New Mexico, Albuquerque, NM, USA

ABSTRACT

Microsystem based piezoelectric kinetic energy harvesters have been extensively investigated over the past decade. The most popular structure of these devices includes a cantilever consisting of a substrate, and a parallel capacitor (electrode/piezoelectric/electrode) layout. This type of structure has the ability to harvest energy by working in the d_{31} mode where the electrical potential is taken in the 3 (out of plane direction) while the strain/stress occurs in the 1 (in plane direction) direction. However, the d_{31} piezoelectric properties are approximately half the value compared to the d_{33} mode. Therefore, operating in the d_{33} mode should result in increased power output. A ferroelectric material that is able to alter its polarity is needed to investigate this potential design enhancement. This paper investigates the performance of both parallel plate capacitor and interdigitated electrode MEMS energy harvesters using lead zirconate titanate thin films using finite element modelling and experimental results to demonstrate the increase in power density, and the effects of varying the electrode configurations and dimensions.

Keywords: Energy Harvester, MEMS, Interdigitated Electrode, Piezoelectric, Parallel Electrode.

NOMENCLATURE

D	electric displacement
d	piezoelectric constant matrix
E	electrical field vector
ε_T	electric permittivity matrix
g	distance/spacing between IDTs
g	acceleration
h	height
n	number of fingers
ρ	density of mass
S	strain vector
s_E	compliance matrix
w	width
T	stress vector
t	thickness
u_i	displacement components, $i = x, y, z$
V	electric potential
x_i	cartesian coordinate axis

1. INTRODUCTION

Microelectromechanical Systems (MEMS) kinetic energy harvesters have been extensively investigated over the past decade. These devices could potentially be used to power wireless sensor networks or low power electronics [1]. Kinetic energy harvesters can use magnetics, triboelectrics, electrostatics, or piezoelectrics. PiezoMEMS energy harvesters are extensively investigated because they offer high voltage output and are easier to fabricate than magnetics, which require deposition of permanent magnets or electrostatics, which often require multiple 3D layers to produce high power. One of the biggest issues with MEMS energy harvesters is the amount of power they can generate, as the power decreases exponentially as devices are scaled down. Therefore, there is a desire to develop new methods of increasing power. Attempts to increase the power have included optimizing piezoelectric properties of the material, but the power figure of merit also includes elastic modulus (stiffer materials generate high power), dielectric constant (lower better) and density. Other attempts to increase power include altering the shape of the cantilever to maximize stress distribution [2, 3] or altering the topography [4].

PiezoMEMS energy harvesters typically use aluminum nitride (AlN [5, 6]), Zinc oxide (ZnO) [7], or lead zirconate titanate (PZT) [8, 9]. However, AlN and ZnO are not ferroelectric so their polarity cannot be altered, and their domains typically need to be aligned in the vertical direction, thus they require a typical parallel electrode configuration. When this type of capacitor structure is deposited onto a common cantilever energy harvester it operates in the d_{31} mode because the strain from the cantilever is perpendicular to the electrodes. However, the d_{31} piezoelectric properties are always less than the d_{33} value (typically about half), therefore resulting in lower efficiency. PZT is ferroelectric and thus it can be polarized to align the domains via poling. Controlling polarity also allows multiple layers of PZT to be integrated to essentially increase the effective

d_{33} properties [10]. Essentially the PZT could be poled along the length of the cantilever by using interdigitated electrodes (IDT) [11-13], so that the energy harvester would work in the d_{33} mode, which should increase the power output.

In this paper we investigate the potential power increase by altering the polarity of the PZT layer and electrode configuration using finite element modelling (FEM) and experimental analysis. We model a single layer of PZT with the same cantilever dimensions but varying electrode configurations and poling orientation. We modelled two different types of PiezoMEMS (parallel plate and IDT) configurations with varying accelerations. The paper goes through a parametric analysis to determine the effects of altering the IDT configurations on voltage output. The results demonstrate that the IDT electrode design generated about 20% higher output voltage than the parallel capacitor-based design. The results indicated that the electrode layout can have a significant effect on the power harvested. The results in this paper are of interest to designers of energy harvesting devices.

2. MATERIALS AND METHODS

2.1 Model Equation

For a piezoelectric material the constitutive equation that couples between electric field and strain is given by

$$S = s_E\, T + d^T E \quad (1)$$

$$D = d\, T - \varepsilon_T\, E_k \quad (2)$$

where S is the mechanical strain, T is the mechanical stress, E is the electric field and D is the electric displacement. s_E is the compliance matrix, d is the piezoelectric constant, ε_T is the electric permittivity matrix. The above form was referred to as the strain charge form of the constitutive relation.

2.2 Computational Domain

2D Meso-Scale Model:

A meso-scale 2D model was used initially to determine the optimal dimensions of the IDT which was based on previous experimental results and comsol models. The overall dimension of the domain for the 2D parallel capacitor and IDT electrode based EH design were 21 $mm \times 2.7\ mm$ as shown in Figs. 1 and 2. Hereafter, the terms "parallel capacitor" and "IDT electrode" were referred to as "parallel" and "IDT" electrode configuration respectively for convenience. The parallel domain (Fig. 1) consists of proof mass placed on the tip of the cantilever beam and the opposite end frame was fixed. Proof mass of 4 mm width and 1.7 mm height was considered. The steel plate was sandwiched between piezoelectric material Lead Zirconate Titanate (PZT 5A) as represented in zoomed view of Fig. 1. The outer layer of the PZT opted as ground while the center layer was output terminal. The IDT based EH design was identical to parallel design except for the electrode configuration as represented in Fig. 2a and 2b. A pair of Pt IDT fingers were named "a" and "b".

3D MEMS Model:

The computational domain of the 3D model for parallel EH design was displayed in Fig. 3. Total inner dimension of the parallel capacitor and IDT domain was $1660\mu m(w) \times 681.57\mu m(h) \times 580\ \mu m(t)$. The MEMS device consisted of a silicon proof mass with dimensions of 360 $\mu m(w) \times 675\ \mu m(h) \times 580\ \mu m(t)$.

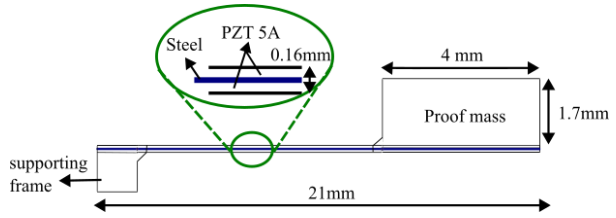

FIGURE 1. COMPUTATIONAL DOMAIN FOR PARALLEL CAPACITOR EH DESIGN.

a)

b)

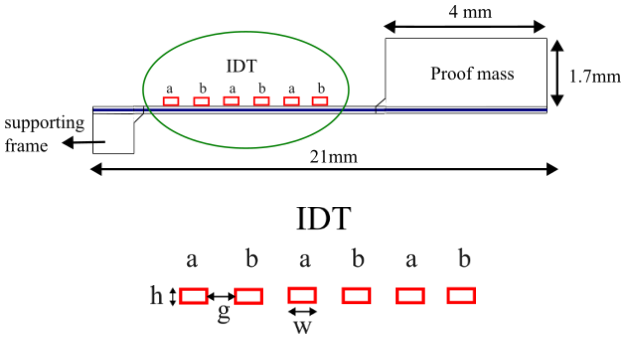

FIGURE 2. COMPUTATIONAL DOMAIN FOR THE a) IDT ELECTRODE EH DESIGN AND b) ZOOMED VIEW OF IDT.

The IDT design for the 3D model was represented in Fig. 4. Dimensions for the IDT design were equivalent to the parallel design except Pt IDT was deposited on layer "7" and electrode layers "6" and "4" were removed as no bottom electrode was necessary. Both parallel and IDT EH designs and dimensions were based on the fabricated device provided by *Radiant Technologies, Inc., Albuquerque, USA*.

2.3 Mesh and Boundary Conditions

Figures 5 shows the example of the computational mesh near the IDT for the 2D model. Mesh details were provided in Table 3. The triangular and tetrahedral mesh was applied for the 2D model and 3D model respectively.

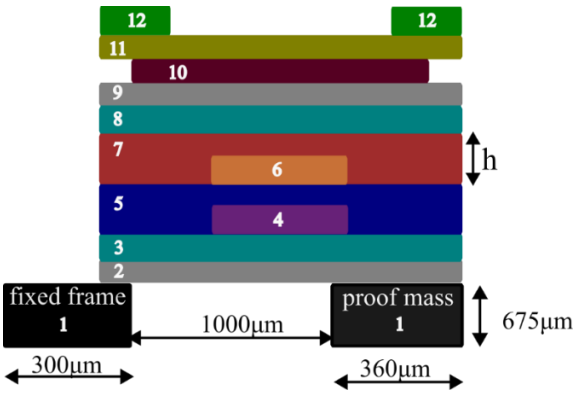

FIGURE 3. CROSS SECTION LAYOUT OF PARALLEL EH MEMS DEVICE.

TABLE 1. LAYER DEPOSTION AND DIMENSION DETAILS.

Number	Layer	Material	Height, *h* *(nm)*
1	Fixed frame	Silicon	675000
1	Proof mass	Silicon	675000
2	Oxide layer	Silicon dioxide	500
3	Oxide layer	Titanium dioxide	40
4	Bottom electrode	Platinum	150
5	Piezoelectric	PZT 52	1000
6	Top electrode	Platinum	100
7	Piezoelectric	PZT 20	250
8	Oxide layer	Titanium dioxide	60
9	Oxide layer	Silicon dioxide	250
10	Metal layer	Magnesium	115
11	Metal layer	Copper	2050
12	Metal layer	Copper	2050

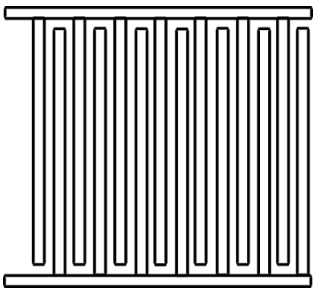

FIGURE 4. IDT DESIGN OF EH FOR 3D MODEL.

A fixed boundary condition was applied to the frame whereas the tip of the cantilever was set free. Boundary load was applied as a function of mechanical acceleration for the entire domain only for frequency response analysis. In the case of the 2D parallel model, exterior and interior surfaces were set as floating potential and ground respectively. For the 2D IDT model, IDT fingers “a” and “b” (from Fig. 2b) were configured as ground and floating potential (output voltage measured) respectively. The same boundary specifications that applied to the 2D model were also implemented to the 3D models of parallel (layers "4" and "6") and IDT design.

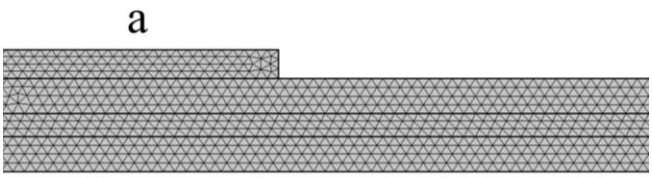

FIGURE 5. MESH FOR THE ZOOMED AREA NEAR IDT FOR 2D MODEL.

TABLE 3. MESH DEATAILS.

	Design	Number of Elements
2D Model	Parallel	72266
	IDT	73756
3D Model	Parallel	340353
	IDT	364103

2.4 Numerical Simulation

Numerical analysis was conducted by FEM using COMSOL Multiphysics software and was subjected to three analyses to find the frequency response of the EH device. The shape function for the dependent electric potential variable was considered quadratic, on the other hand displacement variable was set as quadratic serendipity.

Modal analysis was performed to evaluate the natural frequency of the model. The eigenfrequency solver was set to ARPACK and all other parameters were set to default COMSOL values. Similarly, for frequency analysis MUMPS solver was chosen and the remaining parameters were unchanged.

The piezoelectric properties of the fabricated devices were experimentally determined and inputted into the model to increase accuracy. The d_{33} mode value was experimentally found to be approximately 90 *pC/N*, the d_{31} mode of thin films was not measured but calculated based on the d_{33} value as 55 *pC/N* [11, 12]. The d_{33} piezoelectric properties were found using a Piezometer (PM 300). Mechanical properties such as elastic modulus were determined using nanoindention of the PZT films, and dielectric properties were determined using an LCR meter.

2.5 Microfabrication of PiezoMEMS device

In order to validate the model, we investigated the output of both PiezoMEMS device configurations. The devices were fabricated using Radiant Technologies PiezoMEMS foundry, using the dimensions and thickness described in Table 1 and Fig. 3. The devices were made from a Silicon wafer and consisted of a single active layer of PZT (52/48) and additional insulating layers.

3 RESULTS AND DISCUSSION

The result section was divided into two sections: 3.1) 2D model, 3.2) 3D model and 3.3) experimental results. The 2D EH model was validated against experimental results [13]. The 3D

EH model was based on fabricated devices from Radiant Technologies.

3.1 2D model

Modal Analysis:

Modal analysis was performed to determine the natural frequency of the EH model through Eigenmodes. During this analysis, the device was not subjected to any other forces. Figures 6 and 7 show the modal analysis for parallel and IDT design respectively. The natural frequency for parallel design was found to be 68 Hz and the IDT was 80 Hz. This is due to a change in layers and thickness which affects the overall stiffness.

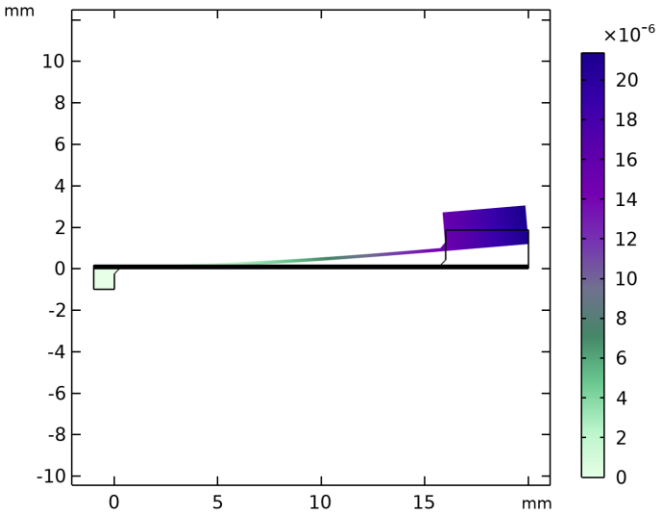

FIGURE 6. MODAL ANALYSIS FOR PARALLEL DESIGN.

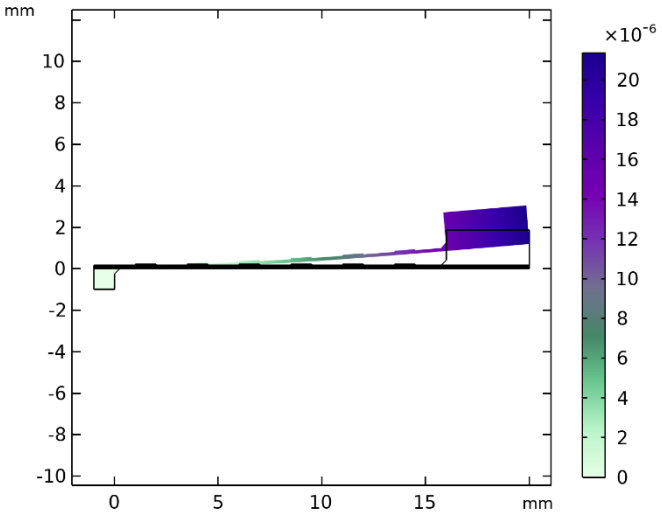

FIGURE 7. MODAL ANALYSIS FOR IDT DESIGN.

Frequency Analysis:

The peak voltage of the EH was measured by conducting frequency analysis under sinusoidal acceleration (0.1-1*g*). The results are displayed in Fig. 8 for parallel and IDT design. The voltage output had a peak value at the resonant frequency which was expected. Peak voltage was found to be maximum for IDT design in comparison to parallel design at the respective natural frequency. Which was in agreement with previous research [11, 12]. It was noticed from the result that the peak voltage for the IDT was 17% higher than the parallel design at their respective natural frequency.

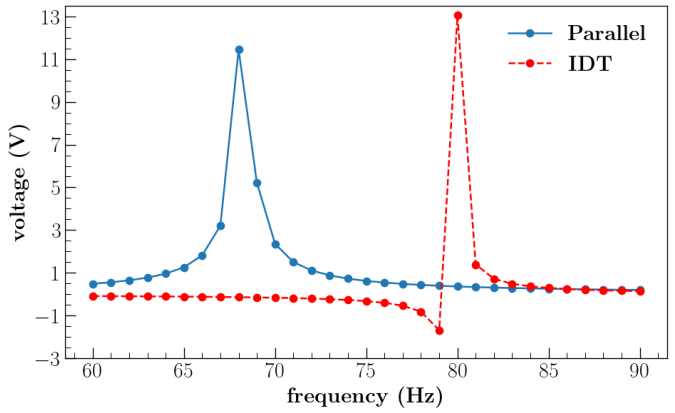

FIGURE 8. 2D MODEL COMPARISION OF OUTPUT VOLTAGE WITH RESPECT TO EXCITATION FREQUENCY FOR PARALLEL AND IDT DESIGN (1g).

Output Voltage vs Acceleration:

EH devices of parallel and IDT design were subjected to mechanical acceleration at the respective frequency (at peak voltage) obtained from frequency analysis. Output voltage varies linearly with respect to acceleration for both designs as shown in Fig. 9. Previous studies indicated a similar linear relationship between voltage and acceleration [11, 12]. The IDT configuration achieved higher voltage output across all accelerations, but it is more significant at higher accelerations.

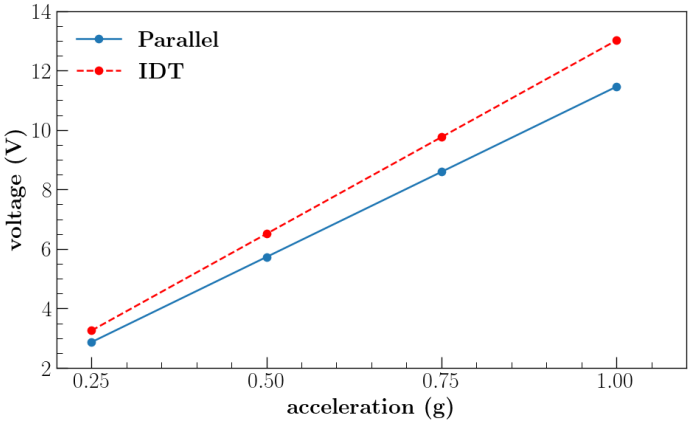

FIGURE 9. 2D MODEL COMPARISION OF OUTPUT VOLTAGE WITH ACCELERATION FOR PARALLEL AND IDT DESIGN AT FREQUECNY 68 Hz AND 80 Hz RESPECTIVELY.

Parametric Studies:

Series of plots from Fig. 10 to 14 display the results of the parametric study for IDT design by varying the finger parameters (width (*w*), gap (*g*), height (*h*), and a number of fingers (*n*)) and analyzed its effect on the output voltage. The device's frequency

response ranged from 60 to 90 Hz in all cases to be consistent with the previous section's result.

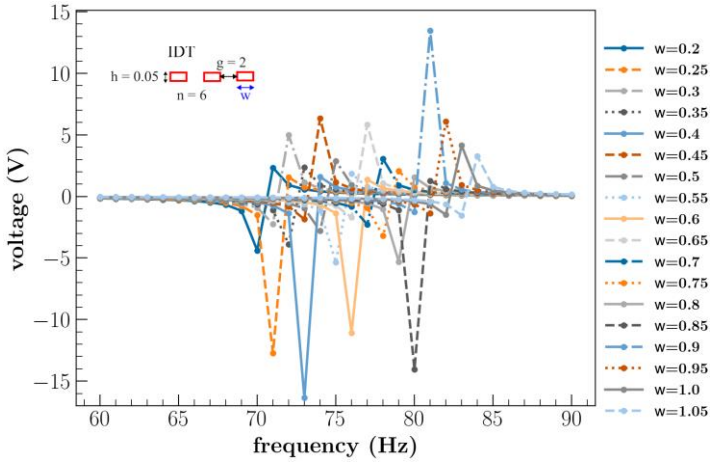

FIGURE 10. 2D MODEL OUTPUT VOLTAGE WITH RESPECT TO VARIATION IN "*w*" (*h*=0.05, *n*=6, *g*=2 DIMENSION IN mm).

As illustrated in Fig. 10, the frequency response at peak voltage shifts to the right side (higher frequency) in relation to an increase in "*w*" of IDT, keeping all other IDT's dimensions unchanged. Peak voltage initially rises with increment in "*w*" up to "*w=0.4 mm*"; after that, it drops and then rises once again after "*w=0.85 mm*". This suggests that higher peak voltage requires an appropriate balance of width for IDT. Similar behavior was noted in Fig. 11 for the increment of "*h*" where other dimensions of IDT's remained constant.

The effect of spacing ("*g*") between IDT fingers on peak voltage was analyzed and results were represented in Fig. 12. All other parameters remained intact. Peak voltage frequency shifted to the left side as "*g*" increased, and the maximum peak voltage occurred at "*g=1.7 mm*". Thus, peak voltage and frequency were affected by the variations of IDT finger spacing.

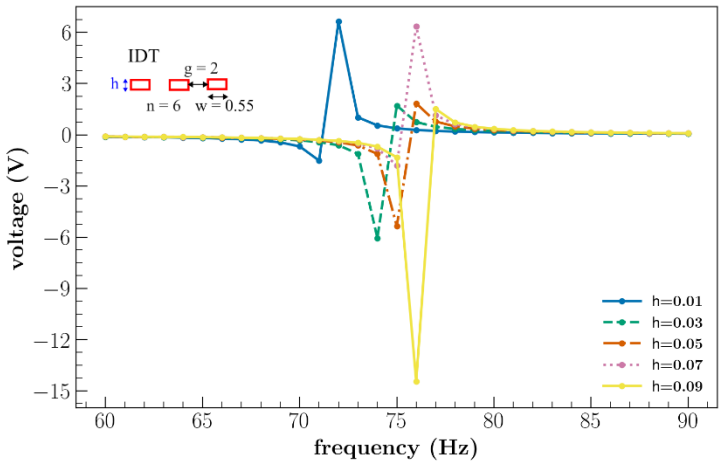

FIGURE 11. 2D MODEL OUTPUT VOLTAGE WITH RESPECT TO VARIATION IN "*h*" (*w*=0.55, *n*=6, *g*=2 DIMENSION IN mm).

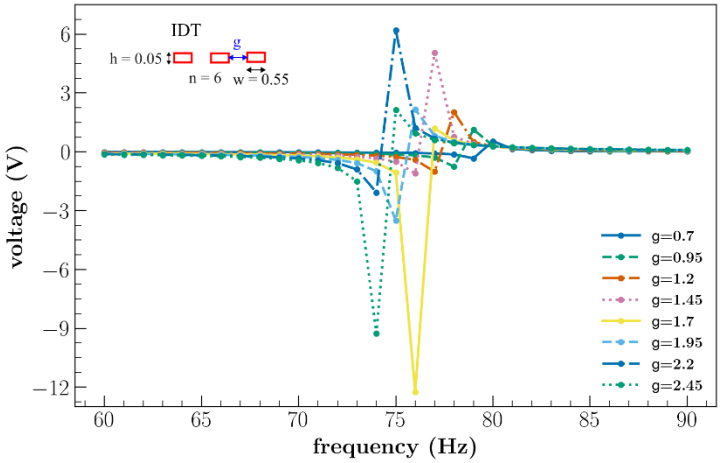

FIGURE 12. 2D MODEL OUTPUT VOLTAGE WITH RESPECT TO VARIATION IN "*g*" (*w*=0.55, *n*=6, *h*=0.05 DIMENSION IN mm).

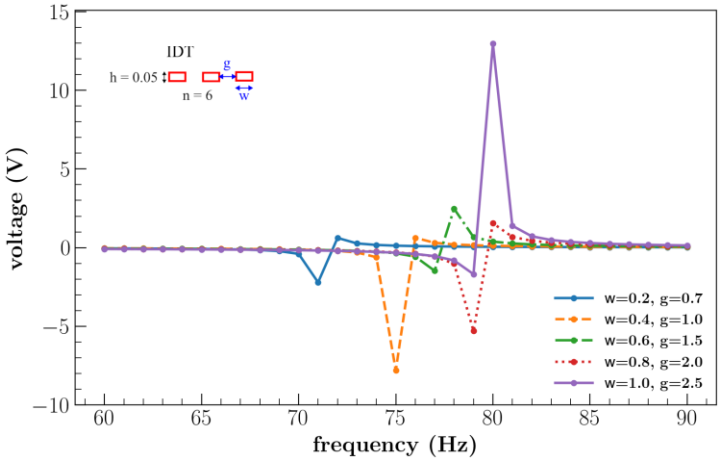

FIGURE 13. OUTPUT VOLTAGE WITH RESPECT TO VARIATION IN "*w*" AND "*g*" (*n*=6, *h*=0.05 DIMENSION IN mm).

It was further investigated the combined effect of parameters "*w*" and "*g*" on peak voltage and frequency and their outcomes was displayed in Fig. 13. Increasing "*w*" and "*g*" together influences the frequency as well as peak voltage where both were increased. Additional study on the number of IDT fingers ("*n*") indicated that peak voltage improved with an increment of "*n*" as shown in Fig. 14. All of the aforementioned parametric simulations demonstrated that the peak voltage and operating frequency of IDT based EH device depend on IDT's design and dimensions. Therefore, optimizing the peak voltage requires using the appropriate IDT's parameter combinations.

3.2 3D model

This section describes and compares the numerical results obtained from the 3D model. A similar procedure followed from the previous section such as modal analysis and frequency response for the 3D model to examine the performance on the parallel and IDT design. Findings were provided in Figs. 15, 16 and 17.

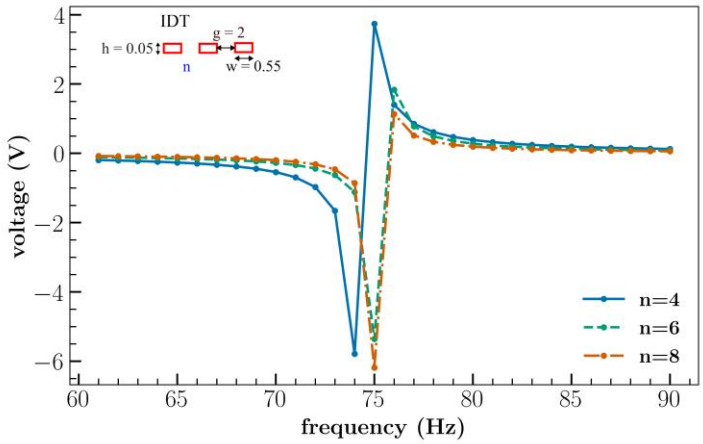

FIGURE 14. 3D MODEL OUTPUT VOLTAGE WITH RESPECT TO VARIATION IN "*n*" (*w*=0.55, *g*=2, *h*=0.05 DIMENSION IN mm).

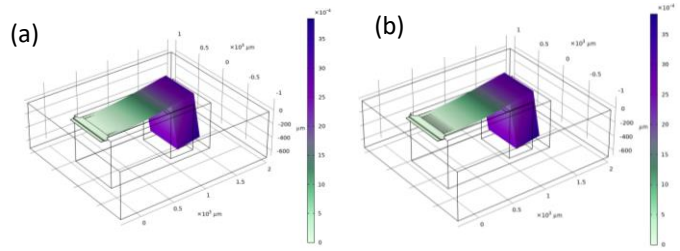

FIGURE 15. MODAL ANALYSIS FOR A) PARALLEL DESIGN AND B) IDT DESIGN.

Modal Analysis:

The natural frequency of the EH model for parallel and IDT was identified using modal analysis with Eigenmodes. The device was not subjected to any additional forces during this study. Figure 15 shows the modal analysis for parallel and IDT design and the natural frequency was found to be 208 Hz and 180 Hz respectively.

Output Voltage vs Acceleration:

The output voltage of the parallel and IDT design was analyzed for increments in acceleration at their corresponding natural frequency that obtained from the modal analysis. Output voltage varies linearly with respect to acceleration for both designs as shown in Fig. 16. A similar tendency of a linear relationship between voltage and acceleration was noticed in comparison with the 2D model. The output voltage was higher for the IDT design, as shown in Fig. 16.

3.3 Experimental Results

Parallel and IDT PiezoMEMS devices were fabricated using Radiant Technologies foundry with the same dimensions in the models. The resonant frequencies of the devices were measured using laser interferometry system (SmarACT) shown in Figure 17. The first mode was found at 196 Hz and 168 Hz for parallel and IDT respectively.

The performance of the devices was determined using a vibration shaker where the peak-to-peak voltage was measured with a load resister matching the cantilever impedance in order to determine power output. The output voltage was higher in both cases than the predicted model, but the trend is similar with the IDT demonstrating significantly higher output voltage. The higher output voltage of the experimental vs. model could be due to stress quality of piezoelectric film or numerous other factors. The power density of the devices at 1 g were 392.4 μW mm^{-3} and 112.1 μW mm^{-3} for the IDT and Parallel devices respectively, which is similar to previous PiezoMEMS[14, 15]. Therefore, the IDT demonstrated more than a 3x increase in power density.

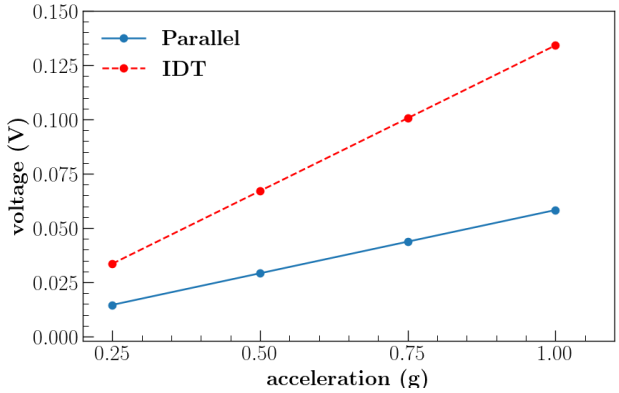

FIGURE 16. 3D MODEL COMPARISION OF OUTPUT VOLTAGE WITH ACCELERATION FOR PARALLEL AND IDT DESIGN AT FREQUECNY 208 Hz AND 180 Hz RESPECTIVELY.

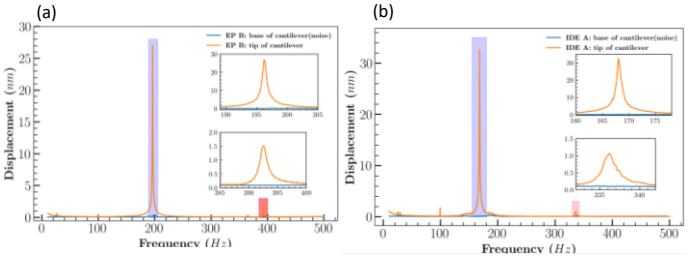

FIGURE 17. EXPERIMENTAL MODAL ANALYSIS FOR A) PARALLEL DESIGN AND B) IDT DESIGN.

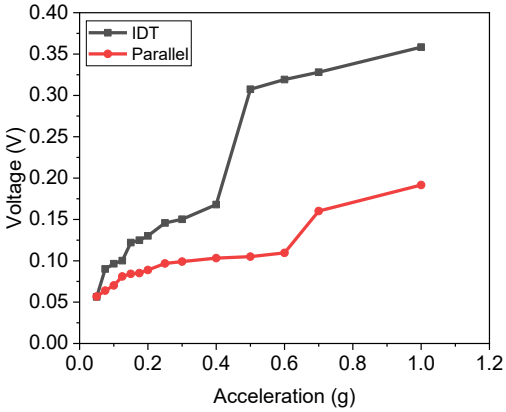

FIGURE 18. EXPERIMENTAL VOLTAGE VS. ACCELERATION.

4 CONCLUSION

In this work, the 2D FEM model was constructed for parallel and IDT design EH based on validated COMSOL model [3] in order to compare the performance of the EH devices depending on d31 and d33 modes. Experimentally measured material properties and values of d33 mode and the calculated value of d31 mode (from Radiant Technologies, Inc., Albuquerque, USA) was applied for both 2D and 3D FEM model. IDT design showed better results in terms of peak voltage with regard to excitation frequency in the case of 2D model. Also, the 2D IDT design displayed increased peak voltage than parallel design when devices were exposed to mechanical acceleration. The results of parametric studies recommended that in order to improve the effectiveness of the IDT device, an appropriate combination of IDT finger design was needed.

Based on the 2D model analysis, an identical simulation was executed for the 3D model that was designed based on the fabricated device. In each analysis, IDT bettered than parallel design. A linear relationship was observed for voltage and acceleration in the case of both 2D and 3D models. Overall, the performance of the EH device could be enhanced with proper IDT design. Future work would involve a series of experiments to validate the FEM simulation and optimize the design.

ACKNOWLEDGEMENTS

This material is based upon work and resources supported by *Radiant Technologies, Inc*. through the DARPA SBIR grant HR001121C0185. The authors would like to thank all members of the SMART Laboratory group at University of New Mexico.

CONFLICT OF INTEREST

The authors have declared no conflict of interest.

REFERENCES

[1] M. Magno, N. Jackson, A. Mathewson, L. Benini, and E. Popovici, "Combination of hybrid energy harvesters with MEMS piezoelectric and nano-Watt radio wake up to extend lifetime of system for wireless sensor nodes," in *26th International Conference on Architecture of Computing Systems 2013*, 2013: VDE, pp. 1-6.

[2] N. Jackson, O. Z. Olszewski, C. O'Murchu, and A. Mathewson, "Shock-induced aluminum nitride based MEMS energy harvester to power a leadless pacemaker," *Sensors and Actuators A: Physical,* vol. 264, pp. 212-218, 2017.

[3] B. Ooi, J. Gilbert, and A. R. A. Aziz, "Analytical and finite-element study of optimal strain distribution in various beam shapes for energy harvesting applications," *Acta Mechanica Sinica,* vol. 32, pp. 670-683, 2016.

[4] T.-T. Yen, T. Hirasawa, P. K. Wright, A. P. Pisano, and L. Lin, "Corrugated aluminum nitride energy harvesters for high energy conversion effectiveness," *Journal of Micromechanics and Microengineering,* vol. 21, no. 8, p. 085037, 2011.

[5] R. Andosca *et al.*, "Experimental and theoretical studies on MEMS piezoelectric vibrational energy harvesters with mass loading," *Sensors and Actuators A: Physical,* vol. 178, pp. 76-87, 2012.

[6] N. Jackson, R. O'Keeffe, F. Waldron, M. O'Neill, and A. Mathewson, "Evaluation of low-acceleration MEMS piezoelectric energy harvesting devices," *Microsystem technologies,* vol. 20, pp. 671-680, 2014.

[7] A. A. Md Ralib, A. N. Nordin, H. Salleh, and R. Othman, "Fabrication of aluminium doped zinc oxide piezoelectric thin film on a silicon substrate for piezoelectric MEMS energy harvesters," *Microsystem technologies,* vol. 18, pp. 1761-1769, 2012.

[8] M.-G. Kang, W.-S. Jung, C.-Y. Kang, and S.-J. Yoon, "Recent progress on PZT based piezoelectric energy harvesting technologies," in *Actuators*, 2016, vol. 5, no. 1: MDPI, p. 5.

[9] D. Shen, J.-H. Park, J. Ajitsaria, S.-Y. Choe, H. C. Wikle, and D.-J. Kim, "The design, fabrication and evaluation of a MEMS PZT cantilever with an integrated Si proof mass for vibration energy harvesting," *Journal of Micromechanics and Microengineering,* vol. 18, no. 5, p. 055017, 2008.

[10] R. Xu *et al.*, "Fabrication and characterization of MEMS-based PZT/PZT bimorph thick film vibration energy harvesters," *Journal of Micromechanics and Microengineering,* vol. 22, no. 9, p. 094007, 2012.

[11] J. C. Park, J. Y. Park, and Y.-P. Lee, "Modeling and characterization of piezoelectric $ d_ {33} $-mode MEMS energy harvester," *Journal of Microelectromechanical Systems,* vol. 19, no. 5, pp. 1215-1222, 2010.

[12] S.-B. Kim, H. Park, S.-H. Kim, H. C. Wikle, J.-H. Park, and D.-J. Kim, "Comparison of MEMS PZT cantilevers based on $ d_ {31} $ and $ d_ {33} $ modes for vibration energy harvesting," *Journal of microelectromechanical systems,* vol. 22, no. 1, pp. 26-33, 2012.

[13] E. Lefeuvre, D. Audigier, C. Richard, and D. Guyomar, "Buck-boost converter for sensorless power optimization of piezoelectric energy harvester," *IEEE Transactions on Power Electronics,* vol. 22, no. 5, pp. 2018-2025, 2007.

[14] N. Jackson, "PiezoMEMS Nonlinear Low Acceleration Energy Harvester with an Embedded Permanent Magnet," *Micromachines,* vol. 11, no. 5, p. 500, 2020.

[15] N. Jackson, O. Z. Olszewski, C. O'Murchu, and A. Mathewson, "Ultralow-frequency PiezoMEMS energy harvester using thin-film silicon and parylene substrates," *Journal of Micro/Nanolithography, MEMS, and MOEMS,* vol. 17, no. 1, pp. 015005-015005, 2018.